nature photonics

Article

https://doi.org/10.1038/s41566-023-01174-4

Onset of vortex clustering and inverse energy cascade in dissipative quantum fluids

Received: 26 May 2022

Accepted: 13 February 2023

Published online: 23 March 2023

Check for updates

R. Panico[1,2], P. Comaron[3,4], M. Matuszewski[3], A. S. Lanotte[1,5], D. Trypogeorgos[1], G. Gigli[1,2], M. De Giorgi[1], V. Ardizzone[1,2], D. Sanvitto[1] ✉ & D. Ballarini[1] ✉

Turbulent phenomena are among the most striking effects that both classical and quantum fluids can exhibit. Although classical turbulence is ubiquitous in nature, the observation of quantum turbulence requires the precise manipulation of quantum fluids such as superfluid helium or atomic Bose–Einstein condensates. Here we demonstrate the turbulent dynamics of a two-dimensional quantum fluid of exciton–polaritons, hybrid light–matter quasiparticles, both by measuring the kinetic energy spectrum and showing the onset of vortex clustering. We demonstrate that the formation of clusters of quantum vortices is triggered by the increase of the incompressible kinetic energy per vortex, showing the tendency of the vortex-gas towards highly excited configurations despite the dissipative nature of our system. These results lay the basis for investigations of quantum turbulence in two-dimensional fluids of light.

The complex dynamics of turbulent flow has repeatedly attracted the interest of scientists across many fields of research[1]. The experimental investigation of quantum fluid dynamics started with the evidence of quantized vortices in superfluid helium[2,3], following the theoretical speculations of Feynman[4]. Although there are important differences, quantum turbulence shares observables with its classical counterpart and allows a simpler description in terms of vortices with unitary topological charge[5,6]. Since the observation of Bose–Einstein condensates (BECs) of ultracold atoms[7,8], BECs have become a well-established platform for the study of quantum turbulence[9,10]. Recently, the ability to form highly oblate BECs boosted the research on vortex clustering[11–16], an elusive feature of two-dimensional quantum turbulence (2DQT) that is strongly related to the inverse energy cascade observed in classical 2D turbulence[17]. The inverse energy cascade, as opposed to the direct cascade, involves energy transfer from small to larger scales and manifests in the universal Kolmogorov-like −5/3 power-law scaling of the kinetic energy spectrum[18]. Onsager proposed an explanation for this counterintuitive phenomenon by applying equilibrium statistical mechanics to a model of point-like vortices: in a closed and conservative system, the formation of vortex clusters is the result of a transition to a thermal equilibrium state that comprises more energy but less entropy (resulting in a negative absolute temperature) as compared to a configuration of randomly distributed vortices[19]. Quantum vortex clustering and negative-temperature regimes were realized only recently in atomic BECs thanks to finely tuned excitation conditions[20,21]. However, the direct measurement of the kinetic energy spectrum and the inverse cascade in 2DQT remains challenging. Optical systems, such as quantum fluids of light, are intriguing alternatives in this regard, as it is possible to directly measure the phase of the quantum fluid and its velocity field[22–26].

As a paradigmatic family of quantum fluids of light, here we study exciton–polaritons—bosonic quasiparticles that result from the strong interaction between light and matter in semiconductor microcavities with embedded quantum wells[27]. The formation of solitons and vortices in polariton superfluids has been observed under different configurations, including spontaneous formation due to local density flows, nucleation in the wake of an obstacle, and direct imprinting via phase mapping[28–31]. Notably, polaritons are strictly 2D, being confined in the plane of the cavity, and the potential landscape can be designed at will by both all-optical and lithographic techniques, potentially enabling strong connections between topological photonics and 2DQT[32–34]. Few works, however, have addressed polariton superfluids in the general

[1]CNR NANOTEC, Institute of Nanotechnology, Lecce, Italy. [2]Dipartimento di Matematica e Fisica E. De Giorgi, Università del Salento, Lecce, Italy. [3]Institute of Physics, Polish Academy of Sciences, Warsaw, Poland. [4]Department of Physics and Astronomy, University College London, London, UK. [5]INFN, Sez. Lecce, Lecce, Italy. ✉e-mail: daniele.sanvitto@cnr.it; dario.ballarini@nanotec.cnr.it

https://doi.org/10.1038/s41566-023-01174-4

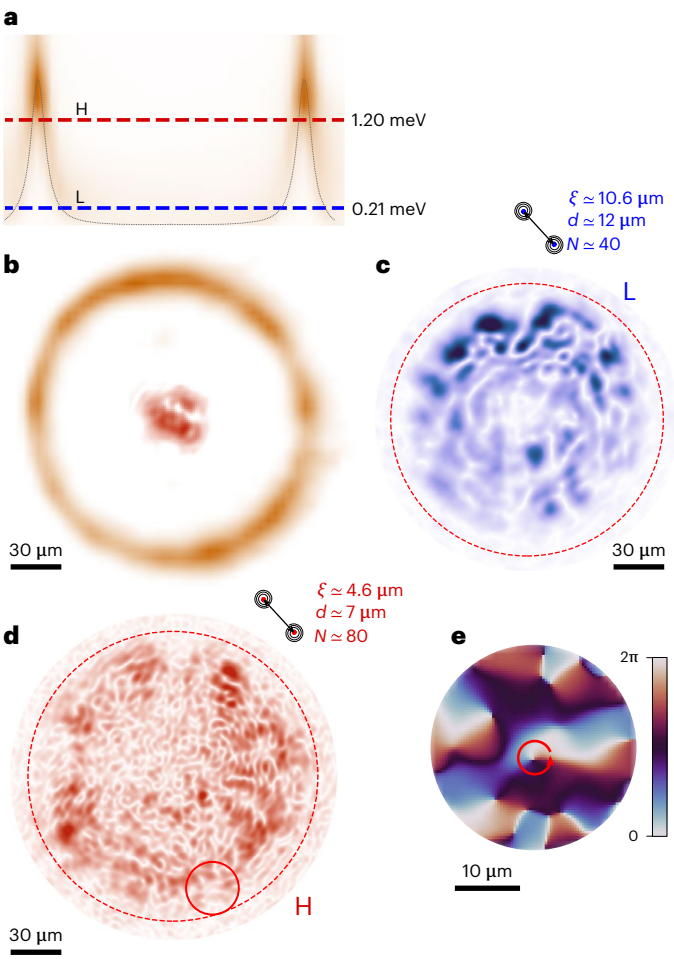

Fig. 1 | Injection and trapping of a polariton quantum fluid. a, Energy-resolved photoluminescence of a vertical slice of the ring-shaped potential barrier, created upon non-resonant excitation of the sample. The blue and red dashed lines indicate the injection energies of the superfluid labelled as L and H, respectively. **b**, Superposition of the image of the trap in real space and the measured density of the polariton superfluid taken 2 ps after injection with a pulsed laser. **c**,**d**, Time frame of the polariton density taken at 60 ps after the injection for low (**c**) and high (**d**) detuning. N denotes the total number of vortices, d the mean distance between nearest-neighbouring vortices and ξ the healing length. The red dashed circle represents the position of the potential barrier. **e**, Phase of the superfluid corresponding to the red solid circle in **d**. Vortices can be identified by a 2π change of the circulation.

context of turbulent dynamics. This is because polariton superfluids, unlike atomic BECs, are inherently dissipative, with the polariton lifetime limited in the picoseconds time range by photon leakage from the microcavity or non-radiative exciton decay. This raises the question of whether 2DQT is even observable in this regime and, in the affirmative case, what are the main differences as compared to a conservative system[35–37]. Theoretically, the turbulent dynamics of out-of-equilibrium condensates were first studied by Berloff[38]. More recently, Koniakhin and colleagues simulated the 2DQT energy spectrum of polariton superfluids in the conservative limit of long polariton lifetime[39]. Despite both these works suggesting that turbulent regimes are indeed possible in polariton fluids, no experimental evidence has been reported so far.

In this Article we show both the onset of vortex clustering and inverse energy cascade in a polariton quantum fluid. To overcome the intrinsic time limit imposed by dissipation, we create a highly energetic initial state by injecting a polariton superfluid against a potential barrier. Indeed, two dynamical processes compete: the build-up of energy at larger spatial scales, and polariton dissipation, which weakens the growth of spatial correlations among vortices. We demonstrate that the initial kinetic energy provided to the superfluid is crucial to form a dense vortex gas and accelerate the formation of clusters. These observations are confirmed using numerical simulations of the polariton nonlinear Schrödinger equation.

System

In quantum fluids, the formation of clusters of same-sign vortices is often seen as the statistical signature of the inverse energy cascade. Indeed, clustering not only limits vortex-pair annihilations and the consequent phonon emission, but drives the system to a highly energetic state[40,41]. To check whether similar dynamics can be observed in a dissipative quantum fluid, the system needs to be initialized in a highly excited state. To this aim, we inject polaritons in a high-Q-factor ($>10^5$) microcavity[42] by using a 2-ps pulsed laser beam focused at the centre of a ring-shaped potential barrier, as shown in Fig. 1a,b (further details are provided in Methods). The detuning of the pulsed beam from the bottom of the potential barrier corresponds to the initial kinetic energy of the polariton fluid, which expands radially after the injection, until it reaches the ring barrier[43,44] (additional details are provided in Supplementary Note 1 and Supplementary Fig. 1). To assess the role of the initial energy on the dynamics of the vortex gas, we consider two injection energies δE from the bottom of the potential, namely $\delta E_{\mathrm{L}} = 0.21$ meV and $\delta E_{\mathrm{H}} = 1.2$ meV, henceforth referred to as L and H, which are indicated in Fig. 1a by the blue and red horizontal dashed lines, respectively. The temporal evolution of the vortex gas after the collision with the potential barrier is followed using off-axis digital holography[45]. This interferometric technique allows us to obtain a time resolution comparable to the pulse length, and enables the direct measurement of both the polariton density and the polariton phase distributions at each time frame with sub-healing-length spatial resolution (additional details are available in Supplementary Note 2 and Supplementary Fig. 2). The vortex dynamics are initiated after an initial expansion time of ~40 ps for the H case and ~50 ps for the slower-expanding fluid in the L case.

A snapshot of the 2D polariton density 60 ps after the injection is shown for the L and H configurations in Fig. 1c,d, respectively. Identification of the vortex positions, including their circulation direction, is realized by searching for an exact 2π circulation of the phase around each point (Fig. 1e). Because the net angular momentum of our experiment is zero, the system nucleates only vortex–antivortex pairs (dipoles), preserving the neutrality of the charge throughout the whole dynamics. In the following we analyse the spatial configuration of the vortex gas and compare its temporal evolution for L and H initial conditions.

Vortex classification and energy decomposition

To study the ordering of our system, we classify the phase singularities into three different categories: free vortices, dipole pairs and clusters of the same sign[12,20,46]. Figure 2a shows a typical result of this analysis applied to a time frame corresponding to 70 ps after the pulsed excitation. The vortex positions are indicated by dots, and the streamlines in the background are the velocity field $\mathbf{v}(\mathbf{r}, t) = \frac{\hbar}{m}\nabla\phi(\mathbf{r}, t)$ with m being the polariton mass, as directly obtained from the measured phase $\phi(\mathbf{r}, t)$ of the polariton fluid. In H, the total number of vortices formed after the collision with the border of the ring is larger (~80) than for L (~40) due to the higher expansion velocity of the fluid. As can be seen from the colour code in Fig. 2a, vortices mostly belong to dipoles in the upper panel (L), in contrast to the lower panel (H), where the number of vortices in clusters, dipoles and free vortices is comparable.

Before discussing the temporal evolution, let us stress the importance of being able to easily measure the phase of the superfluid $\phi(\mathbf{r}, t)$

https://doi.org/10.1038/s41566-023-01174-4

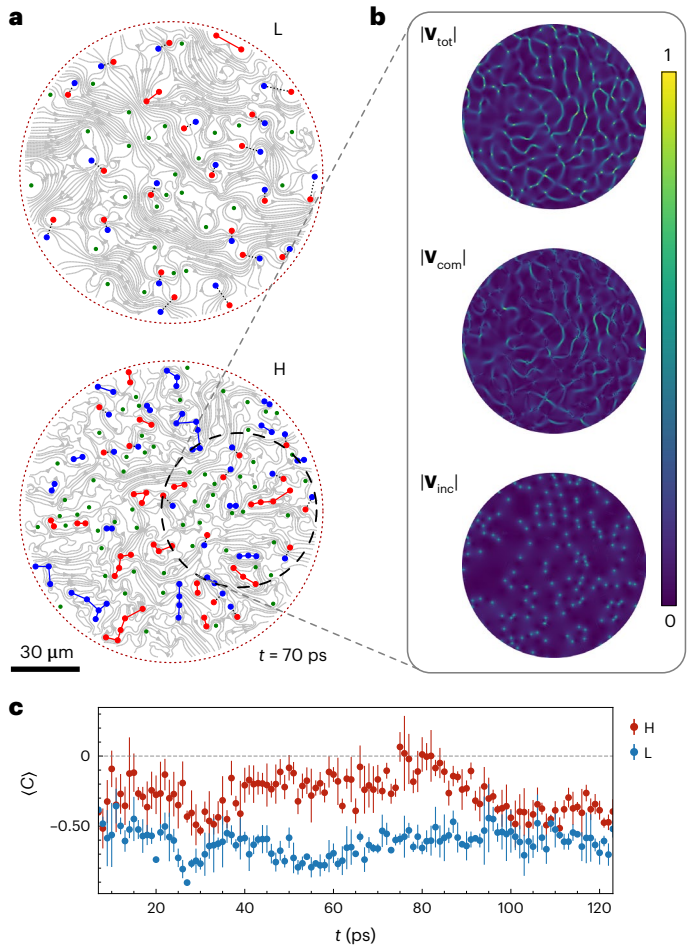

Fig. 2 | Vortex classification and velocity decomposition. a, Distribution of vortices at low (L, top) and high (H, bottom) injection energies taken at $t = 70$ ps after the injection time. Blue and red dots represent positive and negative winding vortices belonging to dipoles (black dotted lines) or clusters (solid lines), respectively. For free vortices (green dots), the sign is not reported. The streamlines in the background show the incompressible velocity field of the superfluid. **b**, Velocity-field decomposition of a portion of the superfluid in **a**. The three figures show the modulus of the total velocity (top), in addition to the compressible (middle) and incompressible (bottom) components. The modulus of the velocity is normalized for each panel. **c**, Vortex first-order correlation functions for high and low injection energy, shown as the mean over different realizations ($n = 4$) by red and blue points, respectively, with their s.d. values.

at any time interval. This allows us to separate the contribution to the total kinetic energy due to the presence of quantum vortices from that coming from the sound waves[47]. Indeed, by applying the Helmholtz decomposition one can separate the divergence-free (incompressible) and the irrotational (compressible) part of the superfluid velocity associated with the vortex distribution and the sound waves, respectively (Supplementary Notes 3 and 4). In the next section we use the incompressible velocity field to compare the information on the kinetic energy with the vortex classification analysis. In Fig. 2b, the results of the velocity decomposition as extracted from the experimental data are shown for a portion of the fluid in H (dashed circle). The bright points in the bottom panel of Fig. 2b correspond to singularities in the polariton phase. In the tracking and classification analysis, we consider only those vortices with cores separated by a distance larger than the healing length, $\xi = \hbar/(2mg|\psi|^2)^{1/2}$, where g is the interaction constant and $|\psi|^2$ is the density of polaritons (Methods).

Temporal evolution and onset of clustering

The vortex tracking allows us to compute the correlation function $C = \frac{1}{N}\sum_{i=1}^{N} c_i$ for each time frame, where N is the total vortex number, and $c_i = 1$ if the circulation of the nearest neighbour of the ith vortex has the same sign, or $c_i = -1$ if it has opposite sign. Increasing values of C correspond to higher energetic states of the vortex gas. In the Onsager model, negative temperatures are associated with $C > 0$, whereas $C = 0$ corresponds to the infinite temperature limit (maximum entropy) and $C = -1$ is the lowest (positive) temperature[14,15,18]. Typically, during spontaneous evolution of a polariton fluid, C is negative and tends towards the lowest energy state, $C = -1$, due to the dissipative nature of the system and the spontaneous nucleation of dipoles (Supplementary Note 5 and Supplementary Fig. 3). In Fig. 2c, we show instead that C reaches values close to $C = 0$ between 40 ps and 80 ps (red points), suggesting that, despite the finite polariton lifetime (~100 ps), the vortex gas evolves towards more energetic configurations. In the dynamical evolution, clustering competes with other processes, the main one being polariton losses, which causes growth of the healing length and makes the inverse cascade even more energetically expensive. In the presence of losses, correlation C initially increases towards higher values and remains approximately constant for a transient time, as shown in Fig. 2c. After 80 ps, dissipation eventually prevails and correlations start decreasing. This behaviour is visible only in H (Fig. 2c, red points), while in L (blue points) the correlation function is $C \approx -0.7$ throughout the dynamics.

The increase of C requires the injection of incompressible kinetic energy into the system. In a closed system such as an atomic BEC, even in the absence of a constant energy injection this is explained by means of an evaporative-heating mechanism[14]. The vortex gas undergoes vortex-pair annihilation while conserving the total energy of the system, leading to an increase of the mean energy per vortex. Therefore, the number of vortices decreases with time, and the few remaining vortices tend to form small clusters[20,48]. In our open system, the simultaneous presence of sound waves and vortices leads to additional mechanisms of energy transfer. In fact, the interplay between the different contributions to the total energy in compressible quantum fluids is crucial to the study of turbulent dynamics, and it has only recently been addressed theoretically[49]. In the following, we show that the kinetic energy of sound waves is efficiently transformed into kinetic energy of the vortex gas.

In Fig. 3a, the ratio of the compressible and incompressible kinetic energy is shown for H and L as a function of time. In H (red points), the compressible component is transformed into incompressible kinetic energy, which becomes dominant starting from 40 ps. In contrast, in L (blue points), the sound-waves component is higher than the incompressible one during the whole dynamics, becoming roughly the same at later times. In Fig. 3b, the three vortex species fractions, namely dipoles (ρ_d), clusters (ρ_c) and free vortices (ρ_f), are shown for the H configuration, along with the total number of vortices (shown as dots). While in the first 40 ps the increase in the incompressible kinetic energy occurs through the nucleation of new vortices, the further increase up to 80 ps occurs with a constant number of total vortices. In this time interval, the increase of the number of clusters occurs at the expense of dipoles, showing that the additional incompressible kinetic energy forces the vortex gas to form small clusters, in contrast to the L configuration (Supplementary Note 6 and Supplementary Fig. 4). This behaviour is displayed in Fig. 3c, where we plot the clustered fraction of vortices versus the average incompressible kinetic energy per vortex, showing the opposite dynamical evolution of the H and L configurations.

Energy spectrum

Figure 4a shows the incompressible kinetic energy spectrum measured in the H and L configurations between 60 ps and 80 ps. The appearance of a Kolmogorov-like $k^{-5/3}$ scaling law (horizontal dashed black line),

https://doi.org/10.1038/s41566-023-01174-4

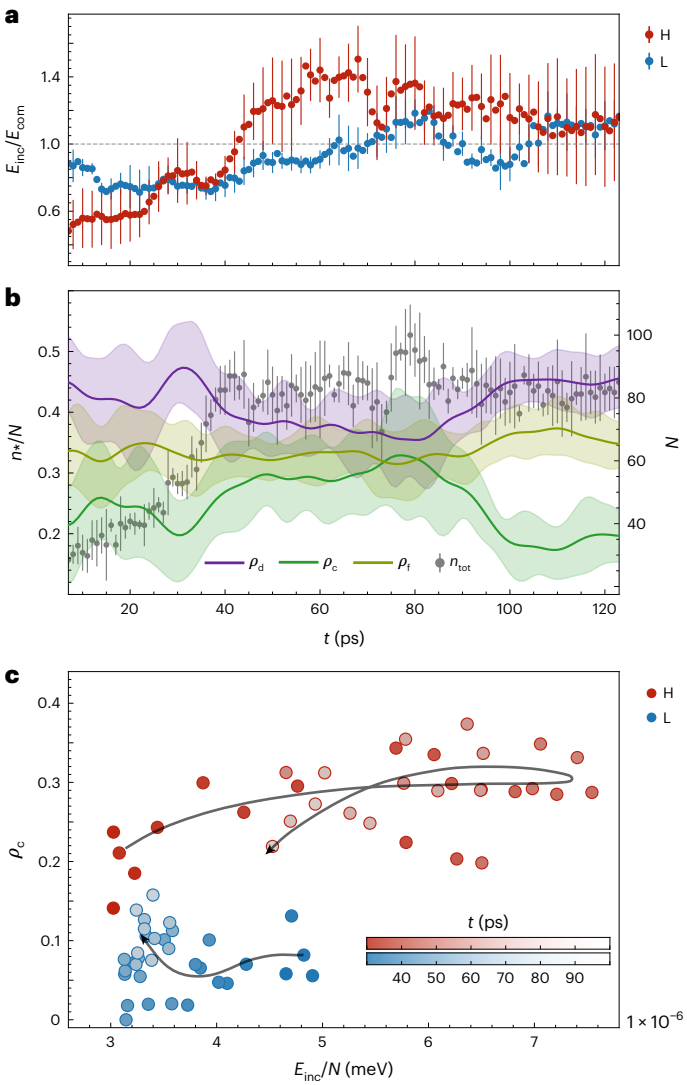

Fig. 3 | Energy transfer and clusterization. a, Ratio between the mean values of the incompressible and compressible kinetic energy for the two configurations, shown as points ± s.d. ($n = 4$). For the sake of clarity, we provide the error bars at each alternate point; the missing ones are comparable to those displayed. **b**, Mean values of the fractions of dipoles (ρ_d, purple line), clusters (ρ_c, green line) and free vortices (ρ_f, yellow green line) for the H configuration (left axis). The temporal resolution is the same as in every other figure and the respective s.d. values are represented by shaded regions. The mean total number of vortices in time is shown by the scatter grey dots with their respective s.d. (right axis). The sample size is the same as in **a**. **c**, Relative number of clusters versus mean incompressible energy per vortex for both the L and H cases. Arrows represent the direction of time.

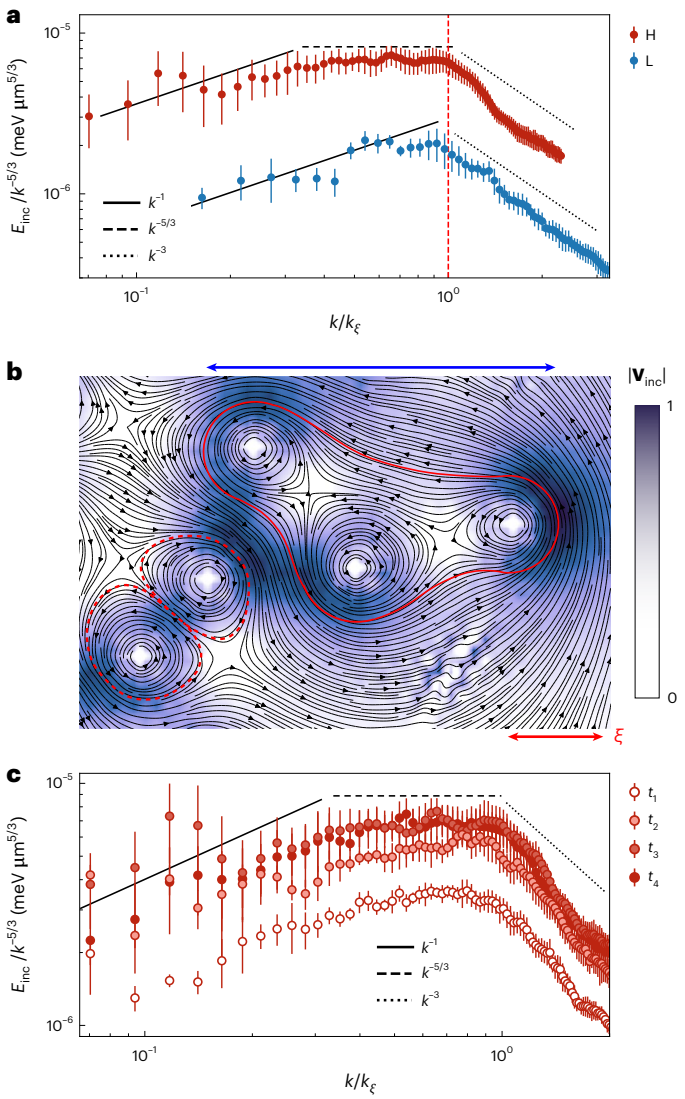

Fig. 4 | Inverse energy cascade. a, Energy spectrum for H (red) and L (blue), integrated in the time interval between 60 ps and 80 ps, reported as mean ($n = 4$) ± s.d. The k axis is rescaled to account for the different healing length (represented by a red dashed line) in H and L (Methods). The black straight lines, which represent the power scaling laws, are just meant as guidelines. **b**, The incompressible velocity field around a configuration made of a dipole (dashed red line) and a cluster of three vortices with the same sign (solid red line). The background heat map represents the modulus of the incompressible velocity. To enhance the visibility, the region close to the vortex core is filtered out and the map is saturated at $|\mathbf{V}_{inc}| = 1.6$ μm ps^{-1}. The 'size' of the cluster, indicated by the blue line, is ~3.4ξ. **c**, Time evolution of the energy spectrum for H, showing the build-up of the inverse energy cascade. The time intervals shown are $t_1 = 34$–44 ps, $t_2 = 47$–57 ps, $t_3 = 60$–70 ps and $t_4 = 70$–80 ps. Error bars are defined as in **a**. All spectra are normalized by the number of particles, as discussed in Methods.

associated with the inverse energy cascade[18,50], is clearly visible in H at wave vectors smaller than k_ξ, the inverse of the healing length. It is noteworthy that, in spite of the small range of scale involved, this is the first direct measurement of an energy spectrum showing the inverse cascade in a 2D quantum fluid.

In the ultraviolet range, $k > k_\xi$, both H and L show a k^{-3} decay (Fig. 4a, dotted black lines), the expected scaling law associated with the internal structure of a quantum vortex[11]. Different behaviours are instead observed for wave vectors smaller than k_ξ. In L, the infrared spectrum ($k < k_\xi$) tends towards k^{-1} (solid black line), which can be derived from the velocity distribution of a collection of vortices in the far-field[11]. In contrast, in H, we observe $k^{-5/3}$ scaling extending from $k_c < k < k_\xi$, with k_c approximately corresponding to the inverse of the typical spatial size of the clusters, $l_c \simeq (3–4)\xi$. In Fig. 4b, to highlight the microscopic mechanism of energy transfer to larger scales, we show the incompressible velocity field, as extracted directly from the experiment in H, around a dipole and a cluster of three vortices. In the dipole, the two vortices are closer to each other, and the maximum of the velocity is observed between them. In the cluster, on the other hand, the velocity field is arranged on a larger spatial scale, with the flow circulating external to the three vortices. Dimensional analysis shows that the time required to form clusters of that size is ~20 ps in our system (Supplementary

Note 7), which is comparable with the measured time interval after the expansion in our measurements. In Fig. 4c, by integrating over different time intervals, we show how the Kolmogorov-like scaling law emerges over time as the energy is gradually transferred to larger scales.

Finally, we note that the energy spectrum is taken directly from spatial differentiation of the measured phase, without any knowledge about the number and relative distances between vortices. The independent observation of vortex clustering and an inverse cascade spectrum provides a direct link between the two descriptions of 2DQT, the one related to the Onsager point-vortex model and that of the inverse cascade of incompressible kinetic energy.

To confirm our findings, we performed simulations of the Gross–Pitaevskii equation for the polariton field[51]. The appearance of the $k^{-5/3}$ scaling law in the incompressible kinetic energy spectrum is observed in numerical simulations and corresponds to an increase of both the correlation function and the incompressible kinetic energy per vortex (Supplementary Fig. 6). As observed in both experiments and simulations, the dynamics is faster when the polariton density is larger and the intervortex distance is comparable to the healing length, resulting in an effective increase of the interactions between vortices. Moreover, we check with simulations that a moderate sample inhomogeneity allows the detection of random vortices, even after averaging over many independent realizations, as already anticipated in previous works[52,53] (further details are provided in Methods and Supplementary Note 9).

In conclusion, in this Article we demonstrate the possibility of exploring turbulent states in quantum fluids of light. These results show the first evidence of the inverse energy cascade in dissipative quantum fluids, along with the onset of vortex clustering on timescales of a few tens of picoseconds. Importantly, we can decouple the compressible and incompressible contributions to the kinetic energy, showing that the energy required to start the clusterization dynamics is provided to the vortex gas by the dissipation of sound waves. Finally, we show that the optical measurement of the velocity field allows unprecedented control over the dynamics of the vortex gas, enabling a new series of experiments to be performed in nonlinear optical systems such as semiconductor microcavities, nonlinear crystals and laser beams coupled to hot atomic vapours or Rydberg atomic states[54–57].

Online content

Any methods, additional references, Nature Portfolio reporting summaries, source data, extended data, supplementary information, acknowledgements, peer review information; details of author contributions and competing interests; and statements of data and code availability are available at https://doi.org/10.1038/s41566-023-01174-4.

References

1. Frisch, U. *Turbulence*: *The Legacy of A. N. Kolmogorov* (Cambridge Univ. Press, 1995).
2. Hall, H. E., Vinen, W. F. & Shoenberg, D. The rotation of liquid helium II II. The theory of mutual friction in uniformly rotating helium II. *Proc. R. Soc. Lond. A Math. Phys. Sci.* **238**, 215–234 (1956).
3. Barenghi, C. F., Skrbek, L. & Sreenivasan, K. R. Introduction to quantum turbulence. *Proc. Natl Acad. Sci. USA* **111**, 4647–4652 (2014).
4. Feynman, R. P. in *Progress in Low Temperature Physics* Vol. 1 (ed Gorter, C. J.) Ch. 2, 17–53 (Elsevier, 1995).
5. Barenghi, C. F. & Parker, N. G. *A Primer on Quantum Fluids* (Springer, 2016).
6. Tsubota, M. Quantum turbulence. *J. Phys. Soc. Jpn* **77**, 111006 (2008).
7. Anderson, M. H., Ensher, J. R., Matthews, M. R., Wieman, C. E. & Cornell, E. A. Observation of Bose-Einstein condensation in a dilute atomic vapor. *Science* **269**, 198–201 (1995).
8. Davis, K. B. et al. Bose-Einstein condensation in a gas of sodium atoms. *Phys. Rev. Lett.* **75**, 3969–3973 (1995).
9. Henn, E. A. L., Seman, J. A., Roati, G., Magalhães, K. M. F. & Bagnato, V. S. Emergence of turbulence in an oscillating Bose-Einstein condensate. *Phys. Rev. Lett.* **103**, 045301 (2009).
10. White, A. C., Anderson, B. P. & Bagnato, V. S. Vortices and turbulence in trapped atomic condensates. *Proc. Natl Acad. Sci. USA* **111**, 4719–4726 (2014).
11. Bradley, A. S. & Anderson, B. P. Energy spectra of vortex distributions in two-dimensional quantum turbulence. *Phys. Rev. X* **2**, 041001 (2012).
12. Reeves, M. T., Billam, T. P., Anderson, B. P. & Bradley, A. S. Inverse energy cascade in forced two-dimensional quantum turbulence. *Phys. Rev. Lett.* **110**, 104501 (2013).
13. Billam, T. P., Reeves, M. T., Anderson, B. P. & Bradley, A. S. Onsager-Kraichnan condensation in decaying two-dimensional quantum turbulence. *Phys. Rev. Lett.* **112**, 145301 (2014).
14. Simula, T., Davis, M. J. & Helmerson, K. Emergence of order from turbulence in an isolated planar superfluid. *Phys. Rev. Lett.* **113**, 165302 (2014).
15. Groszek, A. J., Davis, M. J., Paganin, D. M., Helmerson, K. & Simula, T. P. Vortex thermometry for turbulent two-dimensional fluids. *Phys. Rev. Lett.* **120**, 034504 (2018).
16. Han, J. & Tsubota, M. Onsager vortex formation in two-component Bose-Einstein condensates. *J. Phys. Soc. Jpn* **87**, 063601 (2018).
17. Boffetta, G. & Ecke, R. E. Two-dimensional turbulence. *Annu. Rev. Fluid Mech.* **44**, 427–451 (2012).
18. Kraichnan, R. H. Inertial ranges in two-dimensional turbulence. *Phys. Fluids* **10**, 1417 (1967).
19. Onsager, L. Statistical hydrodynamics. *Il Nuovo Cimento* **6**, 279 (1949).
20. Johnstone, S. P. et al. Evolution of large-scale flow from turbulence in a two-dimensional superfluid. *Science* **364**, 1267–1271 (2019).
21. Gauthier, G. et al. Giant vortex clusters in a two-dimensional quantum fluid. *Science* **364**, 1264–1267 (2019).
22. Arecchi, F. T., Giacomelli, G., Ramazza, P. L. & Residori, S. Vortices and defect statistics in two-dimensional optical chaos. *Phys. Rev. Lett.* **67**, 3749–3752 (1991).
23. Carusotto, I. & Ciuti, C. Quantum fluids of light. *Rev. Mod. Phys.* **85**, 299–366 (2013).
24. Fontaine, Q. et al. Observation of the Bogoliubov dispersion in a fluid of light. *Phys. Rev. Lett.* **121**, 183604 (2018).
25. Ballarini, D. et al. Directional Goldstone waves in polariton condensates close to equilibrium. *Nat. Commun.* **11**, 217 (2020).
26. Öztürk, F. E. et al. Observation of a non-Hermitian phase transition in an optical quantum gas. *Science* **372**, 88–91 (2021).
27. Amo, A. et al. Collective fluid dynamics of a polariton condensate in a semiconductor microcavity. *Nature* **457**, 291–295 (2009).
28. Lagoudakis, K. G. et al. Quantized vortices in an exciton–polariton condensate. *Nat. Phys.* **4**, 706–710 (2008).
29. Sanvitto, D. et al. All-optical control of the quantum flow of a polariton condensate. *Nat. Photon.* **5**, 610–614 (2011).
30. Nardin, G. et al. Hydrodynamic nucleation of quantized vortex pairs in a polariton quantum fluid. *Nat. Phys.* **7**, 635–641 (2011).
31. Panico, R. et al. Dynamics of a vortex lattice in an expanding polariton quantum fluid. *Phys. Rev. Lett.* **127**, 047401 (2021).
32. Ozawa, T. et al. Topological photonics. *Rev. Mod. Phys.* **91**, 015006 (2019).
33. Alyatkin, S., Töpfer, J. D., Askitopoulos, A., Sigurdsson, H. & Lagoudakis, P. G. Optical control of couplings in polariton condensate lattices. *Phys. Rev. Lett.* **124**, 207402 (2020).
34. Pieczarka, M. et al. Topological phase transition in an all-optical exciton-polariton lattice. *Optica* **8**, 1084–1091 (2021).

35. Caputo, D. et al. Topological order and thermal equilibrium in polariton condensates. *Nat. Mater.* **17**, 145–151 (2018).
36. Galantucci, L., Baggaley, A. W., Parker, N. G. & Barenghi, C. F. Crossover from interaction to driven regimes in quantum vortex reconnections. *Proc. Natl Acad. Sci. USA* **116**, 12204–12211 (2019).
37. Zamora, A. et al. Kibble-Zurek mechanism in driven dissipative systems crossing a nonequilibrium phase transition. *Phys. Rev. Lett.* **125**, 095301 (2020).
38. Berloff, N. G. Turbulence in exciton-polariton condensates. Preprint at https://arxiv.org/abs/1010.5225 (2010).
39. Koniakhin, S., Bleu, O., Malpuech, G. & Solnyshkov, D. 2D quantum turbulence in a polariton quantum fluid. *Chaos Solitons Fractals* **132**, 109574 (2020).
40. Skaugen, A. & Angheluta, L. Vortex clustering and universal scaling laws in two-dimensional quantum turbulence. *Phys. Rev. E* **93**, 032106 (2016).
41. Garcia-Orozco, A. D., Madeira, L., Galantucci, L., Barenghi, C. F. & Bagnato, V. S. Intra-scales energy transfer during the evolution of turbulence in a trapped Bose-Einstein condensate. *Europhys. Lett.* **130**, 46001 (2020).
42. Steger, M. et al. Long-range ballistic motion and coherent flow of long-lifetime polaritons. *Phys. Rev. B* **88**, 235314 (2013).
43. Alyatkin, S., Sigurdsson, H., Askitopoulos, A., Töpfer, J. D. & Lagoudakis, P. G. Quantum fluids of light in all-optical scatterer lattices. *Nat. Commun.* **12**, 5571 (2021).
44. Wertz, E. et al. Spontaneous formation and optical manipulation of extended polariton condensates. *Nat. Phys.* **6**, 860–864 (2010).
45. Donati, S. et al. Twist of generalized skyrmions and spin vortices in a polariton superfluid. *Proc. Natl Acad. Sci. USA* **113**, 14926–14931 (2016).
46. Valani, R. N., Groszek, A. J. & Simula, T. P. Einstein-Bose condensation of Onsager vortices. *New J. Phys.* **20**, 053038 (2018).
47. Kolmakov, G. V., McClintock, P. V. E. & Nazarenko, S. V. Wave turbulence in quantum fluids. *Proc. Natl Acad. Sci. USA* **111**, 4727–4734 (2014).
48. Kanai, T. & Guo, W. True mechanism of spontaneous order from turbulence in two-dimensional superfluid manifolds. *Phys. Rev. Lett.* **127**, 095301 (2021).
49. Bradley, A. S., Kumar, R. K., Pal, S. & Yu, X. Spectral analysis for compressible quantum fluids. *Phys. Rev. A* **106**, 043322 (2022).
50. Kolmogorov, A. N. The local structure of turbulence in incompressible viscous fluid for very large Reynolds numbers. *C. R. Acad. Sci. URSS* **30**, 301 (1941).
51. Comaron, P., Carusotto, I., Szymańska, M. H. & Proukakis, N. P. Non-equilibrium Berezinskii-Kosterlitz-Thouless transition in driven-dissipative condensates. *Europhys. Lett.* **133**, 17002 (2021).
52. Lagoudakis, K. et al. Probing the dynamics of spontaneous quantum vortices in polariton superfluids. *Phys. Rev. Lett.* **106**, 115301 (2011).
53. Caputo, D. et al. Josephson vortices induced by phase twisting a polariton superfluid. *Nat. Photon.* **13**, 488–493 (2019).
54. Michel, C., Boughdad, O., Albert, M., Larré, P.-E. & Bellec, M. Superfluid motion and drag-force cancellation in a fluid of light. *Nat. Commun.* **9**, 2108 (2018).
55. Situ, G. & Fleischer, J. W. Dynamics of the Berezinskii-Kosterlitz-Thouless transition in a photon fluid. *Nat. Photon.* **14**, 517–522 (2020).
56. Piekarski, C. et al. Measurement of the static structure factor in a paraxial fluid of light using Bragg-like spectroscopy. *Phys. Rev. Lett.* **127**, 023401 (2021).
57. Clark, L. W., Schine, N., Baum, C., Jia, N. & Simon, J. Observation of Laughlin states made of light. *Nature* **582**, 41–45 (2020).

Methods

Experiment

The ring potential (diameter $R \simeq 150$ μm) was realized by shaping a continuous-wave laser beam ($\lambda = 735$ nm) with a spatial light modulator. The local energy shift of the polariton resonance, due to the high exciton density induced by the continuous-wave pump, was able to confine the polariton superfluid within the potential barrier (Fig. 1a). The polariton superfluid was quasi-resonantly injected ($\lambda \approx 773$ nm) by focusing a pulsed beam (pulse length, ~2 ps) in a Gaussian spot with a beam radius of $w \simeq 17$ μm at the centre of the ring potential (Fig. 1b). Given the repetition rate of the pulsed pump (80 MHz) and the typical integration time of 1 ms, each time frame was obtained from integration of a large number of pulses, giving, as a result, the average vortex distribution averaged over a large number of events. This is required, because a single realization would not provide enough signal to be detected. A time-resolved 2D map of the polariton fluid was obtained by averaging, for each time frame over many pulses, directly on the charge-coupled device camera. The vortex could be detected despite the averaging over many realizations thanks to the unavoidable presence of spatial inhomogeneity, which allows the observation of coherent realizations of the spontaneous vortex dynamics[52] (Supplementary Note 9). Our analysis is the result of an average of four measurements for each case, obtained by translating the sample in plane to exclude effects due to its morphology. Moving onto a different location of the sample, we obtained different spatial configurations, whose statistical properties were, however, unchanged, confirming the statistical significance of the observables. The sample used was a planar Al_xGa_{1-x} As microcavity with aluminium fractions of 0.2 and 0.95 in the distributed Bragg reflectors and 12 quantum wells of GaAs embedded in the cavity layer. The sample was kept at a cryogenic temperature of ~5 K. The measurements were taken in a reflection configuration, with counter-polarized detection with respect to the polarization of the exciting laser. This was possible due to the precession of the polarization typically observed in a polariton microcavity as a consequence of transverse electric–transverse magnetic splitting[58].

From the separation of scales observed in the energy spectrum (Fig. 4a), we were able to estimate the healing length in the 60–80-ps interval to be $\xi \simeq 4.6$ μm in H and $\xi \simeq 10.6$ μm in L.

In the energy decomposition, the density of the system was normalized at each time frame so that $\int \rho(\mathbf{x}) \mathrm{d}\mathbf{x} = 1$, to rule out non-relevant physical behaviours stemming from the modulation of the density throughout the evolution due to the measurement technique employed.

In Fig. 4a, the energy spectrum is displayed for a range of wave vectors spanning from the inverse diameter of the trap, $k_t = 2\pi/R$, to $k_r = 2\pi/r$, with $r = 3$ μm (slightly more than the optical resolution of our optical set-up of ~2 μm), both rescaled by the respective $k_\xi = 2\pi/\xi$ for H and L.

Simulations

To further confirm our findings, we performed simulations of the equations of motion for the polariton field $\psi = \psi(\mathbf{r}, t)$ with the generalized polariton Gross–Pitaevski equation[23,51], which at a mean-field level ($\hbar = 1$) reads as

$$i\mathrm{d}\psi_c = \mathrm{d}t\left[-\frac{\nabla^2}{2m} + g|\psi_c|^2 + \frac{i}{2}\gamma_c + V(\mathbf{r})\right]\psi_c \quad (1)$$

where m is the polariton mass, g is the polariton–polariton interaction strength, and $\gamma_c = 1/\tau_c$ is the polariton loss rate, corresponding to the inverse of the polariton lifetime τ_c. In Supplementary Note 8 we compare and discuss the results obtained with equation (1) with those achieved within the truncated Wigner approximation, a beyond mean-field theoretical formulation that accounts for quantum fluctuations[23].

Parameters were chosen to correspond to the microcavity used in the experiments: $m = 0.22$ ps meV μm^{-2} = 3.5210^{-35} kg and $g = 5 \times 10^{-3}$ meV μm^2. The fluid of light was confined in a hard-bounded annular potential $V(\mathbf{r})$ with radius $r = 70$ μm.

The dynamics was initiated by a central Gaussian profile, providing the initial expansion. Its local phase was constant throughout space, thus accounting for the quasi-resonant nature of the initial experimental impulse. The increase of the detuning of the pump in the experimental case was controlled by the intensity of the initial profile, which also corresponds to an increment of the density of particles as well as the velocity of the outward particle flux. Simulations for different blueshifts were found to be in good agreement with the experimental results, as shown in Figs. 3 and 4 and Supplementary Figs. 5 and 6. In Fig. 3b,c and Supplementary Fig. 6d,e, the fraction of vortices belonging to clusters is shown in experiments and simulations, respectively. On increasing the injection energy, the formation of clusters is faster and occurs with higher probability. The faster dynamics is driven by stronger interactions between vortices, which are effectively increased at lower intervortex distances (that is, when the total vortex density is increased), as observed in both experiments and simulations (Fig. 3b and Supplementary Fig. 6a). The relation between clusterization and vortex density was confirmed by additional analysis, as reported in Supplementary Information.

Data availability

The data that support the findings of this study are available from the authors upon reasonable request.

Code availability

The codes used in this study will be provided upon reasonable request.

References

58. Shelykh, I., Malpuech, G., Kavokin, K. V., Kavokin, A. V. & Bigenwald, P. Spin dynamics of interacting exciton polaritons in microcavities. *Phys. Rev. B* **70**, 115301 (2004).

Acknowledgements

R.P., A.S.L., D.T., G.G., M.D.G., V.A., D.S. and D.B. acknowledge the following projects: Italian Ministry of University (MUR) PRIN project 'Interacting Photons in Polariton Circuits' – INPhoPOL (grant no. 2017P9FJBS); the project 'Hardware implementation of a polariton neural network for neuromorphic computing' – Joint Bilateral Agreement CNR-RFBR (Russian Foundation for Basic Research) – Triennal Program 2021–2023; the MAECI project 'Novel photonic platform for neuromorphic computing', Joint Bilateral Project Italia-Polonia 2022–2023; PNRR MUR project 'National Quantum Science and Technology Institute' – NQSTI (PE0000023); PNRR MUR project 'Integrated Infrastructure Initiative in Photonic and Quantum Sciences' – I-PHOQS (IR0000016); Apulia Region, project 'Progetto Tecnopolo per la Medicina di precisione', Tecnomed 2 (grant no. Deliberazione della Giunta Regionale n. 2117 del 21/11/2018). M.M. and P.C. acknowledge funding from National Science Centre, Poland, grant no. 2016/22/E/ST3/00045. We are grateful to P. Cazzato for valuable technical support during the experiments. D.B. is grateful to B. Alegria for logistics and inspiration.

Author contributions

R.P., P.C., M.M., D.B. and D.S. contributed to the formulation of the project. M.M., D.B. and D.S. supervised the project. R.P. and P.C. contributed to the data curation and, together with A.S.L. and D.B., to the formal analysis and development of the methodology. R.P., P.C. and D.T. cured the codes. Funding acquisition was managed by M.M., D.S. and G.G. All authors contributed to discussions and reviewing the manuscript.

Competing interests
The authors declare no competing interests.

Additional information
Supplementary information The online version contains supplementary material available at https://doi.org/10.1038/s41566-023-01174-4.

Correspondence and requests for materials should be addressed to D. Sanvitto or D. Ballarini.

Peer review information *Nature Photonics* thanks the anonymous reviewers for their contribution to the peer review of this work.